

Thermospheric Density Perturbations Produced by Traveling Atmospheric Disturbances during August 2005 Storm

Kevin Pham¹, Binzheng Zhang¹, Kareem Sorathia², Tong Dang³, Wenbin Wang¹, Viacheslav Merkin², Huixin Liu⁴, Dong Lin¹, Michael Wiltberger¹, Jiuhou Lei³, Shanshan Bao⁵, Jeffrey Garretson², Frank Toffoletto⁵, Adam Michael², and John Lyon⁶

¹National Center for Atmospheric Research

²Johns Hopkins University

³University of Science and Technology of China

⁴Kyushu University

⁵Rice University

⁶Dartmouth College

November 23, 2022

Abstract

Thermospheric mass density perturbations are commonly observed during geomagnetic storms. The sources of these perturbations have not been well understood. In this study, we investigated the thermospheric density perturbations observed by the CHAMP and GRACE satellites during the 24-25 August 2005 geomagnetic storm. The observations show that large neutral density enhancements occurred not only at high latitudes, but also globally. In particular, large density perturbations were seen in the equatorial regions away from the high-latitude, magnetospheric energy sources. We used the high-resolution Multiscale Atmosphere Geospace Environment (MAGE) model to reproduce the consecutive neutral density changes observed by the satellites during the storm. The MAGE simulation, which resolved mesoscale high-latitude convection electric fields and field-aligned currents, and included a physics-based specification of the auroral precipitation, was contrasted with a standalone ionosphere-thermosphere simulation driven by an empirical model of the high-latitude electrodynamics. The comparison demonstrates that a first-principles representation of highly dynamic and localized Joule heating events in a fully coupled whole geospace model such as MAGE is critical to accurately capturing both the generation and propagation of traveling atmospheric disturbances (TADs) that produce neutral density perturbations globally. In particular, the MAGE simulation shows that the larger density peaks in the equatorial region that are observed by CHAMP and GRACE are the results of TADs, generated at high latitudes in both hemispheres, propagating to and interfering at lower latitudes. This study reveals the importance of investigating thermospheric density variations in a fully coupled geospace model with sufficiently high resolving power.

1 Thermospheric Density Perturbations Produced by
2 Traveling Atmospheric Disturbances during August 2005
3 Storm

4 **K. H. Pham¹, B. Zhang^{1,2}, K. Sorathia³, T. Dang⁴, W. Wang¹, V. Merkin³, Huixin Liu⁵, D.**
5 **Lin¹, M. Wiltberger¹, J. Lei⁴, S. Bao⁶, J. Garretson³, F. Toffoletto⁶, A. Michael³, J. Lyon⁷**

6 ¹ High Altitude Observatory, National Center for Atmospheric Research, Boulder, Colorado,
7 USA.

8 ² Department of Earth Sciences, University of Hong Kong, Pokfulam, Hong Kong.

9 ³ Applied Physics Laboratory, Johns Hopkins University, Laurel, Maryland, USA.

10 ⁴ CAS Key Laboratory of Geospace Environment, School of Earth and Space Sciences,
11 University of Science and Technology of China, Hefei, China

12 ⁵ Department of Earth and Planetary Science, Kyushu University, Fukuoka, Japan

13 ⁶ Department of Physics and Astronomy, Rice University, Houston TX

14 ⁷ Thayer School of Engineering, Dartmouth College, Hanover, New Hampshire, USA.

15
16 Corresponding author: Kevin Pham (phamkh@ucar.edu)

17 **Key Points:**

- 18 • Most neutral density peaks observed by CHAMP and GRACE during a geomagnetic
19 storm are associated with traveling atmospheric disturbances
- 20 • TADs generated at high-latitudes propagate globally and interfere to produce large
21 amplitude enhancements at lower latitudes
- 22 • A coupled geospace model with high spatial resolving power is necessary to properly
23 resolve TADs observed by CHAMP and GRACE
24

25 **Abstract**

26 Thermospheric mass density perturbations are commonly observed during geomagnetic storms.
27 The sources of these perturbations have not been well understood. In this study, we investigated
28 the thermospheric density perturbations observed by the CHAMP and GRACE satellites during
29 the 24-25 August 2005 geomagnetic storm. The observations show that large neutral density
30 enhancements occurred not only at high latitudes, but also globally. In particular, large density
31 perturbations were seen in the equatorial regions away from the high-latitude, magnetospheric
32 energy sources. We used the high-resolution Multiscale Atmosphere Geospace Environment
33 (MAGE) model to reproduce the consecutive neutral density changes observed by the satellites
34 during the storm. The MAGE simulation, which resolved mesoscale high-latitude convection
35 electric fields and field-aligned currents, and included a physics-based specification of the
36 auroral precipitation, was contrasted with a standalone ionosphere-thermosphere simulation
37 driven by an empirical model of the high-latitude electrodynamics. The comparison demonstrates
38 that a first-principles representation of highly dynamic and localized Joule heating events in a
39 fully coupled whole geospace model such as MAGE is critical to accurately capturing both the
40 generation and propagation of traveling atmospheric disturbances (TADs) that produce neutral
41 density perturbations globally. In particular, the MAGE simulation shows that the larger density
42 peaks in the equatorial region that are observed by CHAMP and GRACE are the results of
43 TADs, generated at high latitudes in both hemispheres, propagating to and interfering at lower
44 latitudes. This study reveals the importance of investigating thermospheric density variations in
45 a fully coupled geospace model with sufficiently high resolving power.

46 **Plain Language Summary**

47 During geomagnetic storms, increased activity within the geospace environment causes large
48 scale plasma convection to occur and electrons to precipitate into the upper atmosphere. The
49 enhanced heating of the thermosphere by the plasma convection and electron precipitation can
50 produce large perturbations in the neutral density. These neutral density perturbations propagate
51 away from their point of origin, oftentimes traveling to the equator and into the other
52 hemisphere. Simulation results using a high resolution coupled geospace model that includes a
53 magnetosphere, inner magnetosphere, ionosphere, and thermosphere model show that neutral
54 density perturbations generated in one hemisphere can propagate far enough to interfere with
55 those in the other hemisphere. The interference of two or more perturbations produces a region
56 of larger neutral density perturbations. The high resolution coupled geospace model performs
57 significantly better than the standalone model when compared to observations of neutral density
58 by low altitude spacecraft. A significant fraction of the observed neutral density perturbations
59 are captured by the coupled model, especially those are lower latitudes.

60 **1 Introduction**

61 Thermospheric mass density enhancements observed by the Challenging Minisatellite Payload
62 (CHAMP) and the Gravity Recovery and Climate Experiment (GRACE) satellites in the polar cap
63 are well known to be primarily magnetospheric origin. The background neutral density is
64 controlled by solar irradiance while magnetospheric interactions with the solar wind can transport
65 energy along field lines into the ionosphere-thermosphere where they cause neutral density and
66 composition perturbations (Prölss, 2011). During geomagnetic storms, Liu et al. (2010) detected
67 neutral density enhancement events in the polar cap of 90% of the 29 storms with $Dst < -100nT$

68 that were examined, indicating that neutral density enhancements in the polar cap are not rare.
69 Understanding the source of and magnetospheric impact on the density enhancements is crucial to
70 the magnetosphere-ionosphere-thermosphere (MIT) coupling physics, and has been a long-
71 standing issue.

72
73 Prior studies have examined the neutral density enhancements and the associated Joule heating
74 imposed by magnetospheric energy input. Electromagnetic energy dissipated as Joule heating in
75 the upper atmosphere is related to the amount of downward Poynting flux, especially in regions of
76 high conductance (Kelley et al., 1991; Richmond 2010; Vanhamki, et c., 2012). However, the
77 spatial distribution of large-scale density enhancements does not correlate well with the
78 distribution of Poynting flux (Billett et al., 2021) and nearly 50% of polar cap density
79 enhancements events do not have concurrent increases in energy input as seen in field-aligned-
80 current (FAC) structures (Liu et al., 2010). Bruinsma and Forbes (2007, 2009) and Lu et al. (2016)
81 found that polar cap mass density enhancements could arise from passage of traveling atmospheric
82 disturbances (TADs) that have propagated across the polar cap and subsequently toward the
83 equator, suggesting that direct energy inputs at the density enhancement location is not required.
84 In fact, density and temperature enhancements have been found to not occur right at the location
85 of the strongest Joule heating, but rather regions of strong downwelling of the air (Burns et al.,
86 1995; Wang et al., 2012). Heating of the thermosphere can produce TADs, which are associated
87 with transient neutral density structures (e.g., Forbes et al., 2005; Bruinsma and Forbes, 2010) that
88 perturb the background neutral density as TADs propagate equatorward with speeds near the local
89 sound speed and are also frequently observed in the mid- and low- latitudes (Mayr et al., 1990;
90 Bruinsma and Forbes, 2009, and references therein).

91
92 The source, properties, and evolution of neutral density perturbations and TADs are not easily
93 addressed with limited in-situ observations (Bruinsma and Forbes, 2009). Extensive modeling
94 work has been performed to improve the description of storm-time thermospheric heating resulting
95 from the interaction with the magnetosphere, including improved empirical specifications
96 (Weimer, 2005), data assimilation models (Lu et al., 2016), or coupling to physics-based
97 magnetosphere models (e.g., Connor et al., 2016; Wang et al., 2004). Other attempts to reproduce
98 neutral density perturbations have added additional physics to coupled MIT models such as soft
99 precipitation (Zhang et al., 2012; Deng et al., 2013), and Alfvén wave heating (Hogan et al., 2020).
100 These have all demonstrated some success in capturing statistical properties (Zhang et al, 2012;
101 Deng et al., 2013) or longer duration orbit averages (Lei et al., 2010; Hogan et al., 2020) of neutral
102 density enhancements observed by CHAMP. While coupled models produce neutral density
103 enhancements more self-consistently, the transient nature and timescale of TADs and associated
104 perturbations require sufficient model resolution and an accurate representation of the relevant
105 physical processes to resolve the localized generation and propagation of TADs. Therefore, a
106 detailed comparison with the data and successful capture of the density structures along each
107 satellite orbit has not been achieved by simulations to our best knowledge. Increased resolution is
108 necessary in the magnetosphere-ionosphere models to improve the structure of high-latitude FAC
109 (Honkonen et al., 2013; Wiltberger et al., 2017) to better represent the location and strength of
110 Joule heating and thus the generation of TADs. High resolution thermosphere-ionosphere models
111 also can better represent mesoscale structures of Joule heating (Matsuo and Richmond, 2008) and
112 improve their capability to resolve the propagation of TADs and their associated density structures
113 (Dang et al., 2018). Therefore, a coupled MIT model capable of properly capturing the generation,

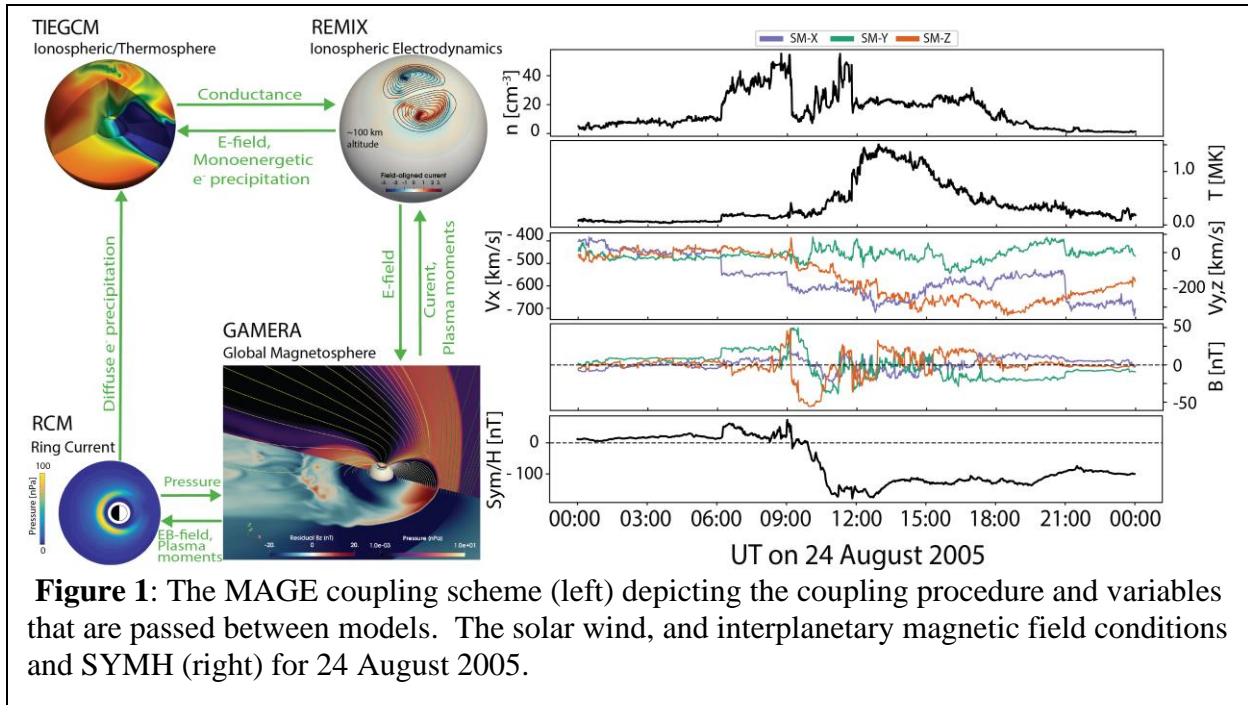


Figure 1: The MAGE coupling scheme (left) depicting the coupling procedure and variables that are passed between models. The solar wind, and interplanetary magnetic field conditions and SYMH (right) for 24 August 2005.

114 resolution, and transport of TADs is critical to understanding thermospheric neutral density
 115 enhancements produced by TADs.

116
 117 Using a coupled geospace model with high spatial resolving power, we demonstrate that a
 118 significant number of density enhancements seen by satellites along satellite orbits at all latitudes
 119 during a single storm on 24 August 2005 are actually TADs that were generated at high-latitudes.
 120 The Multiscale Atmosphere Geospace Environment (MAGE) model used in this study couples
 121 multiple first-principles, high-resolution models of different geospace domains together into a
 122 cohesive geospace model and represents a significant advancement in modeling the geospace
 123 environment. We also demonstrate that a coupled geospace model with high-resolution is critical
 124 in simulating the TAD properties and ultimately, whether the neutral density enhancements as
 125 measured by CHAMP and GRACE are captured by the model.

126 2 Model Description

127 This study uses the current iteration of the MAGE model which two-way couples the Grid
 128 Agnostic MHD Environment for Research Applications (GAMERA) global magnetospheric MHD
 129 model (Zhang et al., 2019a; Sorathia et al., 2020), the Rice Convection Model (RCM) (Toffoletto
 130 et al., 2003), the Thermosphere-Ionosphere Electrodynamic General Circulation Model
 131 (TIEGCM) (Richmond et al., 1992; Qian et al., 2014), and the RE-developed Magnetosphere-
 132 Ionosphere Coupler/Solver (REMIX), which is a rewrite of the MIX code (Merkin and Lyon,
 133 2010). A schematic of how the components of the MAGE model are coupled together and the
 134 input solar wind/interplanetary magnetic field conditions for both the MAGE model and the
 135 WEIMER empirical high-latitude convection model (Weimer, 2015) that is used to drive the
 136 standalone TIEGCM for the 2005 August 24 event can be found in Figure 1a.

137
 138 The CHAMP and GRACE observations of the 2005 August 24 geomagnetic storm have been
 139 previously studied at length (e.g., Crowley Krauss et al., 2015; Oliveira and Zesta, 2019). Crowley

140 et al. (2010) simulated 3 CHAMP orbits near the start of the storm using AMIE as the high latitude
141 driver and saw some improvement in capturing density enhancements near the cusp. However,
142 their simulation struggled to capture the amplitude of the enhancement and variability. Krauss et
143 al. (2018) found that while the CHAMP and GRACE spacecraft are at similar altitudes, the amount
144 of orbital decay experienced during this storm is extremely different, with CHAMP experiencing
145 up to 3 times larger orbital decay than GRACE. The large difference in orbital decay throughout
146 this event presents a challenge to global models to capture the characteristics seen by both satellites
147 simultaneously.

148
149 GAMERA solves the single fluid magnetohydrodynamic equations using a 7th-order
150 reconstruction scheme on a nonorthogonal-structured grid that has 192, 192, and 256 cells in the
151 radial, meridional and azimuthal directions, respectively. This maps approximately 600km
152 resolution in the plasmashet. The grid places higher resolution in important magnetospheric
153 regions such as the bow shock, magnetopause, plasmashet, and near the low-altitude (inner)
154 boundary. The combination of a high order reconstruction scheme with aggressive flux limiting
155 is key to properly resolving the generation and transport of structures with a minimal number of
156 cells (Zhang et al., 2019a).

157
158 At the inner boundary of GAMERA, the grid maps to approximately 0.5° in the polar ionosphere
159 which is also the chosen resolution for the REMIX grid. REMIX solves Poisson's equation to
160 obtain the electrostatic potential. The monoenergetic precipitation is calculated from MHD
161 parameters following the Zhang et al. (2015) formulation. To represent the diffuse precipitation,
162 we integrate the electron channels in RCM to obtain the electron flux in the loss cone, thus
163 improving upon the MHD specification of Zhang et al. (2015) by including the RCM drift physics.
164 The REMIX grid is 0.5° in latitude and longitude with low-latitude boundary at 45° magnetic
165 latitude. This translates to 90 and 720 cells in the latitudinal and longitudinal directions,
166 respectively. RCM solves the bounce-averaged drift motion of ions and electrons in the inner
167 magnetosphere with 180 and 361 cells in latitudinal and longitudinal directions and 115 energy
168 channels each for ions and electrons. TIEGCM solves for the chemistry and dynamics of both
169 neutrals and ions in the upper atmosphere ranging from 97km up to approximately 500km at solar
170 min and 700km at solar max. The high-resolution TIEGCM applies ring-average filtering (Zhang
171 et al., 2019b) to increase the resolution a globally uniform 0.625° in both latitudinal and
172 longitudinal directions (Dang et al., 2021). The vertical resolution of the TIEGCM is a quarter of
173 a scale height. This translates to 288, 576, and 57 cells in latitude, longitude, and altitude,
174 respectively.

175
176 Typically, when not coupled to a magnetospheric model, high-latitude convection in TIEGCM is
177 specified by either Weimer (Weimer, 2005) or Heelis (Heelis et al., 1982) empirical models. For
178 this study, the neutral densities from the standalone TIEGCM driven by the widely used Weimer
179 empirical model is contrasted with MAGE results to provide a clear example of improvements
180 enabled by a comprehensive geospace coupled model. The Weimer model is widely used as the
181 empirical specification for the high latitude convection of choice for most of the thermosphere-
182 ionosphere models within the community (Krall et al., 2014; Fok et al., 2014; Guo et al., 2019),
183 including the standalone TIEGCM (Qian et al., 2014). In addition, the electron precipitation
184 calculated based on MHD parameters in MAGE are also significantly more self-consistent and
185 dynamic than those specified in the standalone TIEGCM (Roble and Ridley, 1987). We denote

186 the run where the standalone TIEGCM was driven by the Weimer model to be simply the
187 WEIMER run.
188

189 While the storm occurred on 2005 August 24, the model runs started on 2005 August 23 at 12 UT
190 to provide ample time to precondition the models properly. Because 2005 August 23 has relatively
191 quiet conditions, we opted to only show results for 2005 August 24. During this event, both
192 CHAMP and GRACE spacecraft were present and together, cover two different local times (LT).
193 The neutral densities derived from CHAMP and GRACE (Sutton, 2011) were mapped to 400km
194 altitude by assuming diffusive equilibrium at a constant temperature using the MSIS model. The
195 MAGE and WEIMER results extracted at the CHAMP and GRACE positions at 400km altitude
196 are compared to the derived neutral densities.

197 3 Results

198 The cross polar cap potential (CPCP) for the northern (Figure 2a) and southern (Figure 2b)
199 hemispheres from MAGE is significantly dynamic, consistent with the changes in solar wind
200 conditions shown in Figure 1. Similarly, the MAGE simulated hemispherically integrated Joule
201 heating (JH, Figure 2c and 2d) also shows strong temporal variations. For comparison, the CPCP
202 and Joule heating in the standalone TIEGCM driven by the Weimer model are also shown in Figure
203 1. The temporal trends of these two parameters from the two model outputs are similar, which is
204 not surprising as they correlate with the solar wind driving. The CPCP from MAGE is persistently
205 higher than WEIMER's CPCP, consistent with prior works using MHD models of the
206 magnetosphere (e.g., Connor et al., 2016; Wiltberger et al., 2017; Mukhopadhyay et al., 2021).
207 Other data-based methods such as AMIE and SuperDARN also persistently underestimate the
208 CPCP as measured by DMSP (Kihn et al., 2006; Xu et al., 2008). Additionally, while the difference

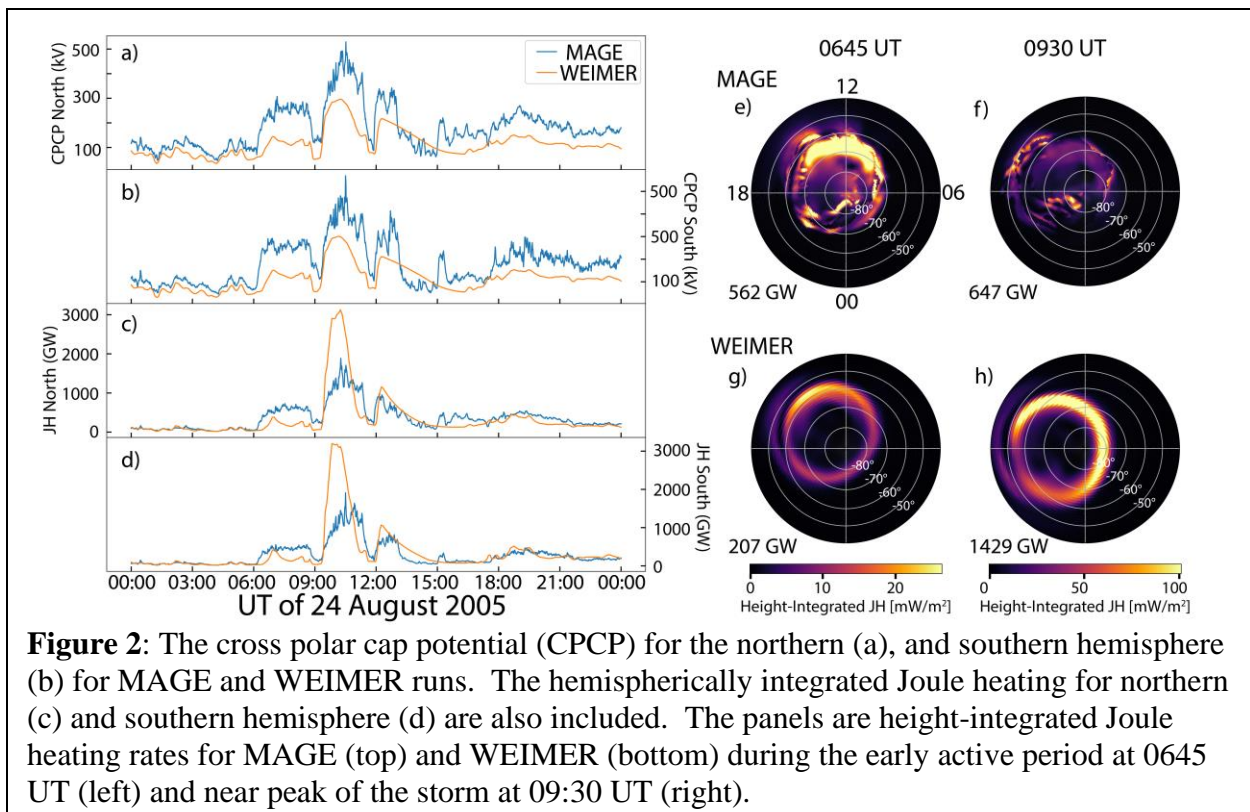
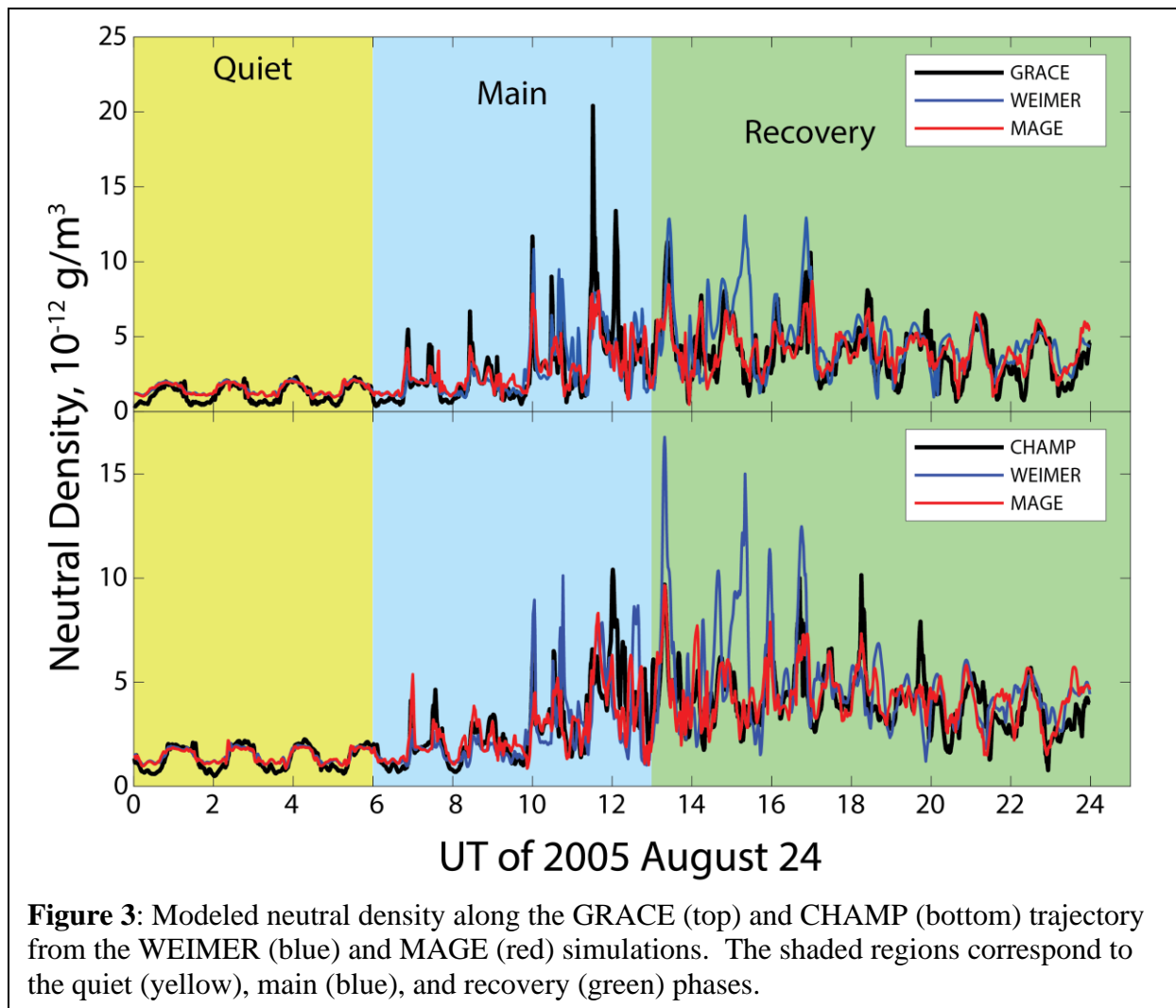


Figure 2: The cross polar cap potential (CPCP) for the northern (a), and southern hemisphere (b) for MAGE and WEIMER runs. The hemispherically integrated Joule heating for northern (c) and southern hemisphere (d) are also included. The panels are height-integrated Joule heating rates for MAGE (top) and WEIMER (bottom) during the early active period at 0645 UT (left) and near peak of the storm at 09:30 UT (right).

209 in CPCP is larger during active periods, the resulting JH into the ionosphere-thermosphere in the
210 coupled MAGE was actually lower than WEIMER. The difference between JH and CPCP trends
211 is most likely a result of differing electric fields between the models and the underlying
212 conductance distributions. This reflects the complexity and intertwined nature of the coupled
213 system and the need for a coupled model to better capture the intricacies of the MIT coupling.
214 This also indicates that global parameters such as CPCP may not fully capture the localized and
215 dynamic nature of the regional mesoscale structures of Joule heating, which is determined by the
216 strength of electric fields and the ionospheric conductivity strongly regulated by particle
217 precipitation at a particular location. This is further illustrated in the right-hand side top panels in
218 Figure 2, which show the JH distribution calculated by MAGE during the early main phase (07
219 UT) and late main phase (10 UT) during the storm event. We note above that the JH distribution
220 and structure includes contributions from electron precipitation by enhancing ionospheric
221 ionization and conductivity, with the auroral arc associated with diffuse electron precipitation
222 appearing prominently in MAGE results. During the early main phase, MAGE Joule heating
223 distribution contained many localized heating zones which contributes to a large hemispherically
224 integrated power of 472 GW. During the later main phase, the MAGE JH behaved
225 similarly with significantly finer detail and mainly localized heating regions. Note that the color
226 scales are different for these two subplots. The hemispherically integrated Joule heating rate at
227 this time is 1266 GW. The bottom panels show the Joule heating patterns from the Weimer run
228 which were much smoother with large broad structures due to its empirical and statistical nature,
229 with a total JH of 382 GW and 2910 GW at two UTs, respectively. Note that Weimer JH was
230 smaller than that in MAGE in the early main phase, but is over a factor of two larger in the later
231 phase. This difference is significant for locations and amplitudes of storm-time TADs that are
232 generated at high-latitude by thermospheric temperature changes associated with Joule heating as
233 shown below.

234
235 A comparison of the 1-minute modeled neutral density at 400km with the observation derived
236 density data along the CHAMP and GRACE tracks is given in Figure 3 for both MAGE and
237 WEIMER (Figure 3) runs. MAGE is able to capture both the variability and magnitude of the most
238 of the neutral density enhancements. To better quantitatively describe the data-model performance,
239 we split the event into three parts as shaded in Figure 3: the quiet conditions (yellow), the storm
240 main phase (blue), and the recovery phase (green). The quiet period is defined as everything before
241 the sudden storm commencement (SSC) at 6 UT. In this period, CHAMP and GRACE observed
242 less and very minor enhancements in the neutral densities; we consider everything after the SSC
243 is part of the storm main phase until the DST trends upwards at 13:00 UT; and the recovery phase
244 is everything afterwards until the end of the day. Table 1 summarizes how well the models (MAGE
245 and Weimer) perform compared with the CHAMP and GRACE observations.

246
247 During the quiet period, there are no large density enhancements along the tracks, and it is difficult
248 to identify any discernable differences between the models. Earlier in the main phase, MAGE
249 captures density enhancements near 07:30, 08:20, and 09:00 UT, which WEIMER almost all
250 misses. During the most active period, WEIMER performs poorly by both overestimating the
251 observed enhancements and also generating enhancements that are not observed, while MAGE
252 captures a significant fraction of the observed enhancements. The recovery phase exhibits a
253 similar trend, with WEIMER performing especially poor between 15:00 UT through 18:00 UT.
254 Overall, MAGE matches the morphology of neutral density and magnitude of the enhancements
255 observed by CHAMP and GRACE significantly better than WEIMER.



256

257 Note here that TIEGCM is the I-T model with 0.625° resolution that is used for both MAGE and
 258 Weimer runs. The difference between the two runs is that MAGE uses convection pattern and
 259 precipitation that is self-consistently calculated within a fully coupled whole geospace model,
 260 including the interaction between solar wind and the magnetosphere, magnetosphere dynamics,
 261 ring current and precipitation, and their electrodynamic coupling with the I-T, whereas high
 262 latitude inputs in Weimer run are empirically specified. This demonstrates the importance of
 263 having not only high resolution, but also an accurate physics description of the MIT coupling to
 264 capture the storm-time temporospatial variability in the I-T system with high fidelity. This point
 265 is further illustrated in Figure 4.

266

267 While agreement with observed neutral densities during the quiet and late recovery phases can be
 268 easily seen in Figure 3, agreement and details of where disagreements occur are difficult to
 269 ascertain from Figure 3. Examining a shorter period spanning 09:00 UT and 17:00 UT, and with
 270 the orbital latitude (Figure 4) reveals that WEIMER tends to generate neutral density perturbations
 271 in the northern high latitude, when none are observed, for instance at 15:15 UT for both
 272 CHAMP and GRACE data, and it also overestimates the perturbations seen in the southern
 273 hemisphere. On the other hand, MAGE captures CHAMP and GRACE reasonably well at all

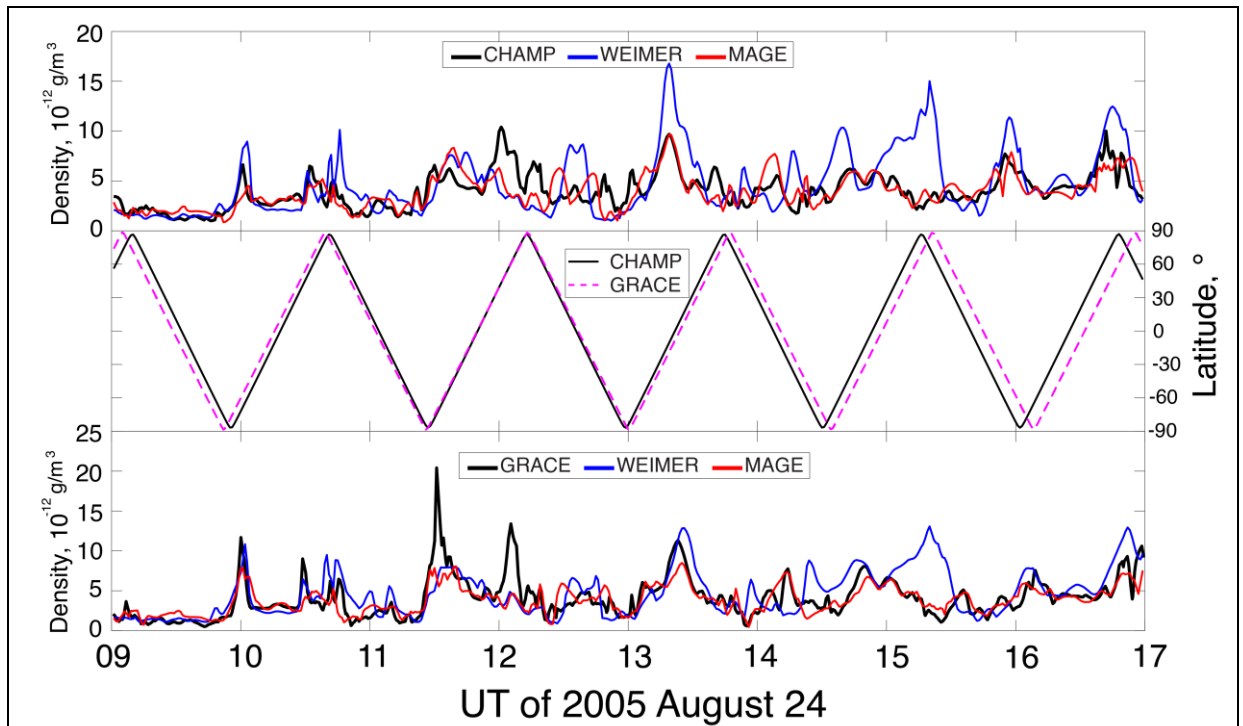
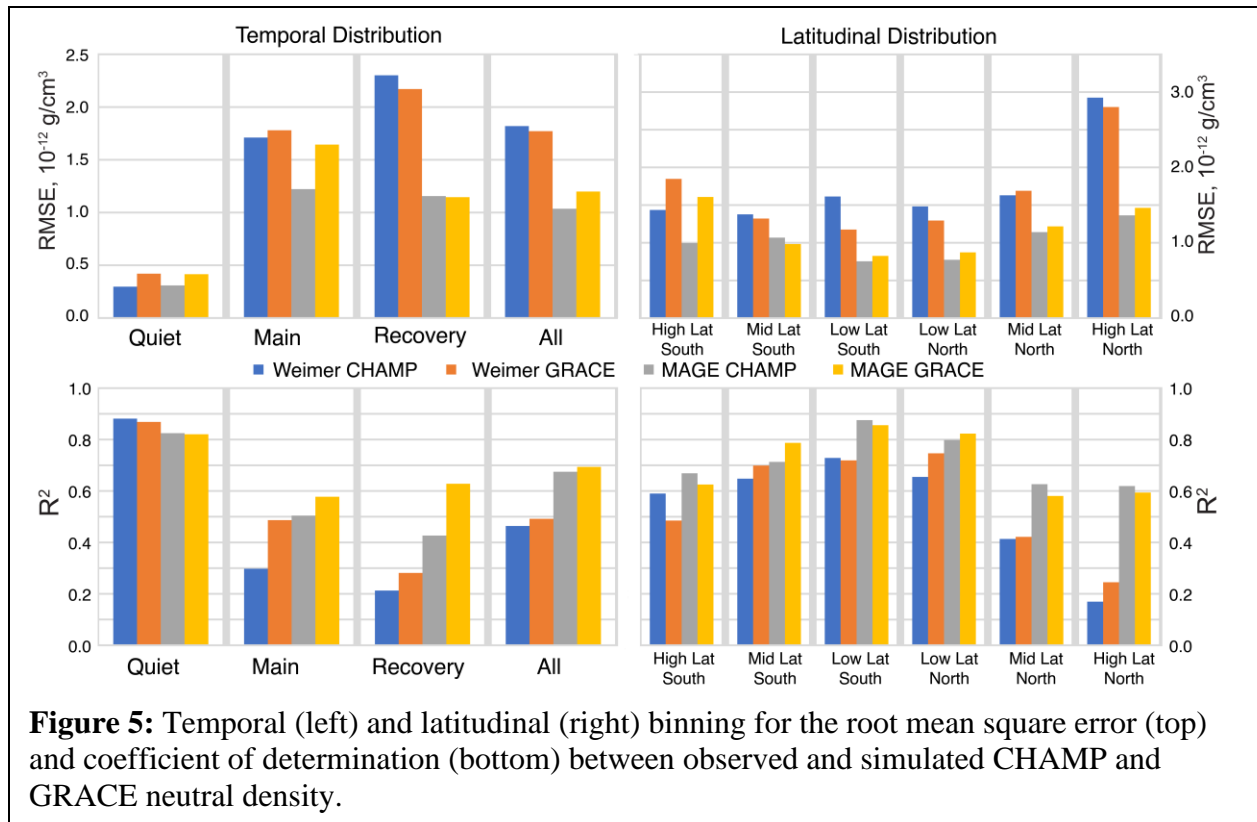


Figure 4: Modeled neutral density along the CHAMP (top) and GRACE (bottom) orbit from the WEIMER (blue) and MAGE (red) simulations. The orbital latitude (middle) for CHAMP (solid) and GRACE (dashed) are also shown.

274 latitudes for this geomagnetic storm. The larger and non-localized Joule heating from WEIMER
 275 (Figure 2) produces neutral density perturbations with incorrect propagation speeds and
 276 amplitudes, resulting in variability and perturbations at the lower latitudes to not be properly
 277 simulated. There are two large density peaks in GRACE data, one at 11:40 UT near the southern
 278 cusp and one at 12:05 UT near the northern cusp, are not captured by the MAGE.
 279

280 An animation of the global neutral density distribution at 400km simulated by MAGE with virtual
 281 CHAMP and GRACE positions marked is shown in Movie S1 in the Supporting Information.
 282 While perturbations in the neutral density during quiet times occur, the perturbations are small in
 283 amplitude and agreement with the background neutral density dominates the root mean square
 284 error (RMSE) and coefficient of determine (R^2) calculation (Figure 5). During periods of more
 285 activity, plasma convection and auroral precipitation in the high-latitudes are significantly
 286 enhanced and greatly influence the neutral density. The heating also generates TADs that
 287 propagate away from the high-latitudes, and in some cases, reach the other hemisphere. When the
 288 TADs intersect with the CHAMP and GRACE trajectory, the satellites observe a local neutral
 289 density enhancement. While the WEIMER simulation captures and most of the time overestimates
 290 a few of the larger TADs observed by CHAMP and GRACE, MAGE captures significantly more
 291 TADs, especially the smaller amplitude ones. Since these observed density enhancements are the
 292 intersection of a propagating TAD and a moving spacecraft (CHAMP or GRACE), to simulate
 293 these density enhancements at that exact moment suggests that the TADs were both generated at
 294 the correct time and location, and also propagated with the correct speed to reach the spacecraft
 295 location at the right moment as observation. We note that both models are unable to capture the
 296 very large enhancements seen by GRACE during the storm main phase near 11:30 UT and 12:00
 297 UT. Examination of Movie S1 show that these very large enhancements occur when GRACE is



298 flying through the cusp region in the southern and northern hemispheres, respectively. Cusp soft
 299 precipitation (Zhang et al., 2012) and Alfvénic wave heating (Hogan et al., 2020) have not yet
 300 been implemented in the MAGE model which are likely the reason that the model misses these
 301 two outstanding density enhancements as thermospheric heating associated with these processes
 302 have been proposed to be an important process for local density perturbations (Zhang et al., 2012;
 303 Deng et al., 2013; Hogan et al., 2020).

304
 305 The RMSE and R^2 between both models and the CHAMP and GRACE observations (Figure 5)
 306 quantify the overall model performance. The RMSE gives us a sense for how close the results are
 307 in value. While the R^2 value is a good measure of how the model captures the temporal morphology
 308 of the CHAMP and GRACE neutral densities, it does not necessarily account for any offsets or
 309 how close the model agrees with the actual measured value. Therefore, using RMSE and R^2 in
 310 combination provides a better sense of model performance than if either of them was used on its
 311 own. When the RMSE and R^2 are binned based on geomagnetic activity throughout the day
 312 (Figure 5, left), we find that during quiet conditions the heating in the ionosphere-thermosphere is
 313 not as significant as during active times, so both models perform equally well there. During the
 314 main phase, the empirical specification from WEIMER is smoother and less dynamic than the
 315 physics-based MAGE model. This results in both a different total Joule power and a much
 316 smoother distribution without localized structures than MAGE. How this impacts model
 317 performance is reflected in significantly worse RMSE for WEIMER compared to MAGE for the
 318 main phase where WEIMER has 40% and 8% larger errors than MAGE for the CHAMP and
 319 GRACE tracks, respectively. In addition, R^2 shows that MAGE improves upon WEIMER in the
 320 ability to capture the morphology by 70% and 19%, respectively. While both model runs similarly
 321 lack the necessary heating in the cusp region, the whole geospace model of MAGE performs well

322 in capturing both the amplitudes, locations and timing of the observed density perturbations,
323 indicating the necessity of using first principles whole geospace models such as MAGE to describe
324 the storm-time behavior of the whole system and its temporal and spatial variability of different
325 scales.

326 The recovery phase is vastly more complex than the main phase. The RMSE and R^2 for both
327 WEIMER and MAGE are worse in the recovery phase than the main phase. With an inner
328 magnetosphere model to provide a dynamic plasmasphere and ring current in the coupled MAGE
329 model, the more realistic recovery phase produces a 100% better improvement across the board
330 compared to WEIMER's RMSE and R^2 . As seen in the RMSE and R^2 when the whole run ("All")
331 is analyzed, the good performance during the quiet phase makes both model results appear to agree
332 better with CHAMP and GRACE than they really are. However, it is still clear from analyzing
333 "All" that MAGE is a significant improvement over statistical empirical specification of high
334 latitude inputs using Weimer. Including a coupled model allows for the magnetosphere to impact
335 the dynamic changes in the thermosphere-ionosphere and vice versa, for more self-consistent
336 thermospheric heating, in the coupled MAGE reproduces well the morphology (as determined by
337 R^2) and magnitude (as determined by RMSE) of the neutral density as observed by CHAMP and
338 GRACE.

339
340 To better understand how differing high latitude dynamics impact the global thermosphere-
341 ionosphere, we bin the CHAMP and GRACE comparisons into bins of 30° widths (Figure 5, right).
342 Here, both the RMSE and R^2 provide the same conclusion: MAGE performs significantly better
343 in the high latitude northern hemisphere. Since only the high latitude are different between the
344 models, the poorer performance in the mid and low latitudes by Weimer compared to MAGE is
345 entirely due to the overestimated energy input by WEIMER (Figure 2) at the high latitudes
346 propagating towards and impacting all other latitudes.

347
348 On a more local scale, we focus on two significant neutral density enhancements seen by CHAMP
349 that occurs at 07:00 UT and 13:20 UT. The panels in Figure 6 show CHAMP clearly flying
350 through TADs at these times. We note that GRACE had already flown through the TAD at 07:00
351 UT a few minutes prior and it would fly through the 13:20 UT TAD approximately 10 minutes
352 later. Figure 6c shows the MAGE simulated difference in neutral density every minute along 12:00
353 LT, which is close to the CHAMP trajectory. This clearly highlights the neutral density
354 perturbations associated with the TADs. By backtracking the perturbations occurring at 07:00 UT
355 and 13:20 UT in Figure 6c, we find that the first neutral density enhancement at 07:00 UT was
356 measured shortly after the TAD was generated near -60° LAT around 0645 UT in the southern
357 hemisphere.

358 On the other hand, the second neutral density enhancement at 13:20 UT was generated much earlier
359 near 09:30 UT at the northern high-latitudes. Snapshots from Movie S2 are shown in Figure 7
360 show a neutral density crest at the high-latitudes in the northern hemisphere that propagates to
361 lower latitudes for many hours. By the time the crest has reached the equator and into the southern
362 hemisphere where it is observed by CHAMP at 13:20 UT, the neutral density perturbation has
363 significantly increased in amplitude after it intersected with a norward propagate TAD from the
364 southern hemisphere. Many of other large lower latitude enhancements such as enhancement at
365 CHAMP at 13:20 UT are also from TADs generated in either high-latitudes and have increased in
366 amplitude by intersecting with other TADs as it propagates to lower latitudes, to produce a
367 significantly larger perturbation away from the high-latitude TAD source regions.

368

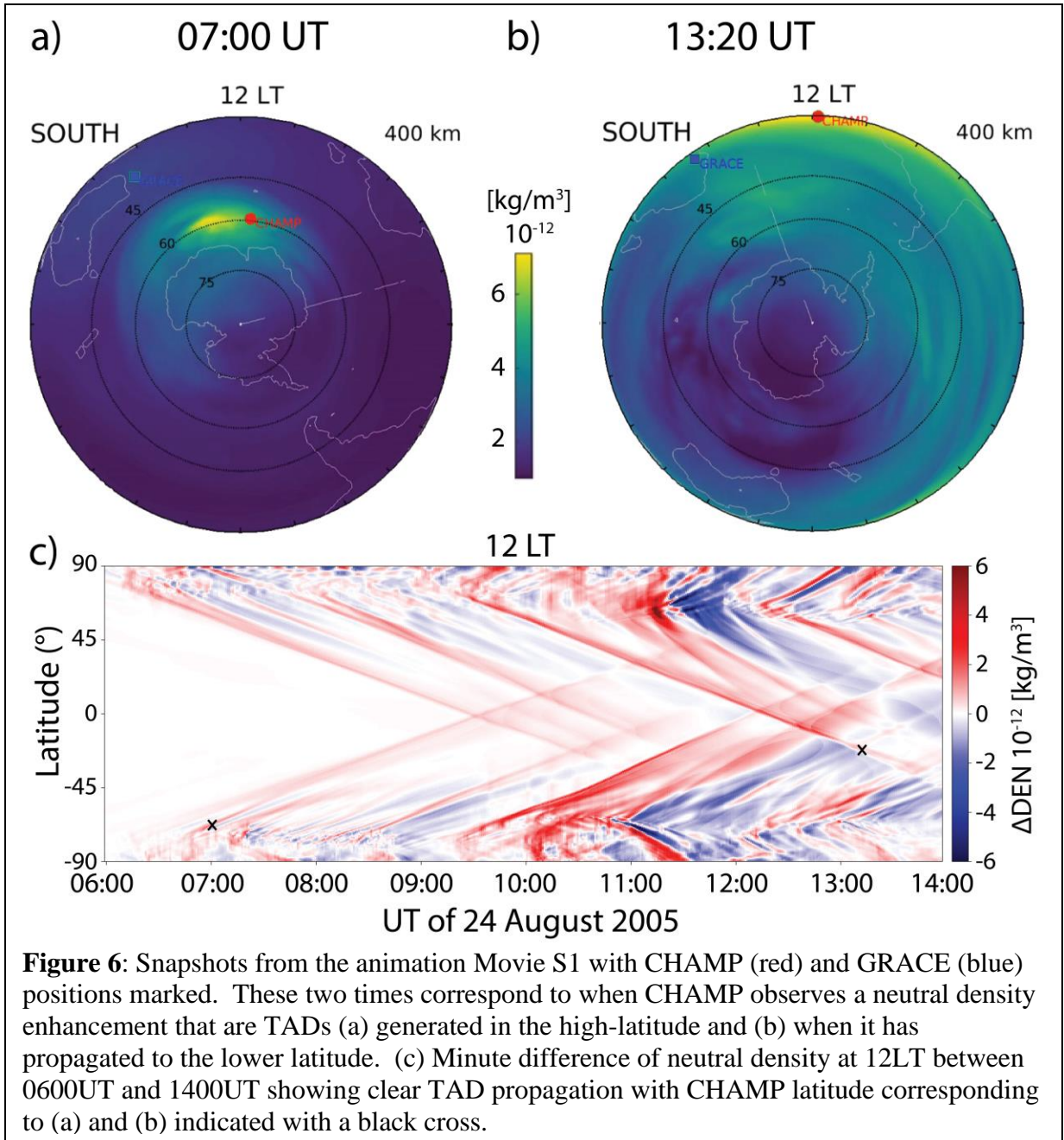


Figure 6: Snapshots from the animation Movie S1 with CHAMP (red) and GRACE (blue) positions marked. These two times correspond to when CHAMP observes a neutral density enhancement that are TADs (a) generated in the high-latitude and (b) when it has propagated to the lower latitude. (c) Minute difference of neutral density at 12LT between 0600UT and 1400UT showing clear TAD propagation with CHAMP latitude corresponding to (a) and (b) indicated with a black cross.

369 Due to the many small and medium scale TADs at the higher latitudes, it is difficult to track the
 370 large-scale TADs to the exact moment they were generated but following the propagation in both
 371 the Movie S1 and Movie S2, we estimate the generation of the 07:00 UT and 13:20 UT
 372 enhancements occurred at 06:45 UT and 09:30 UT, respectively. The height-integrated JH at both
 373 06:45 UT and 09:30 UT were previously shown in Figure 2. The height-integrated JH at 06:45
 374 for both MAGE and WEIMER are distributed in approximately the same latitudinal and
 375 longitudinal regions. Both show an enhanced JH region near 15 LT. However, because 06:45 is
 376 near the start of the main phase, heating from WEIMER ramps up more slowly, but it is much
 377 faster in the coupled MAGE, leading to more heating in the MAGE run. This produces a TAD
 378 with larger amplitude than that found in WEIMER, and more closely matches with GRACE and

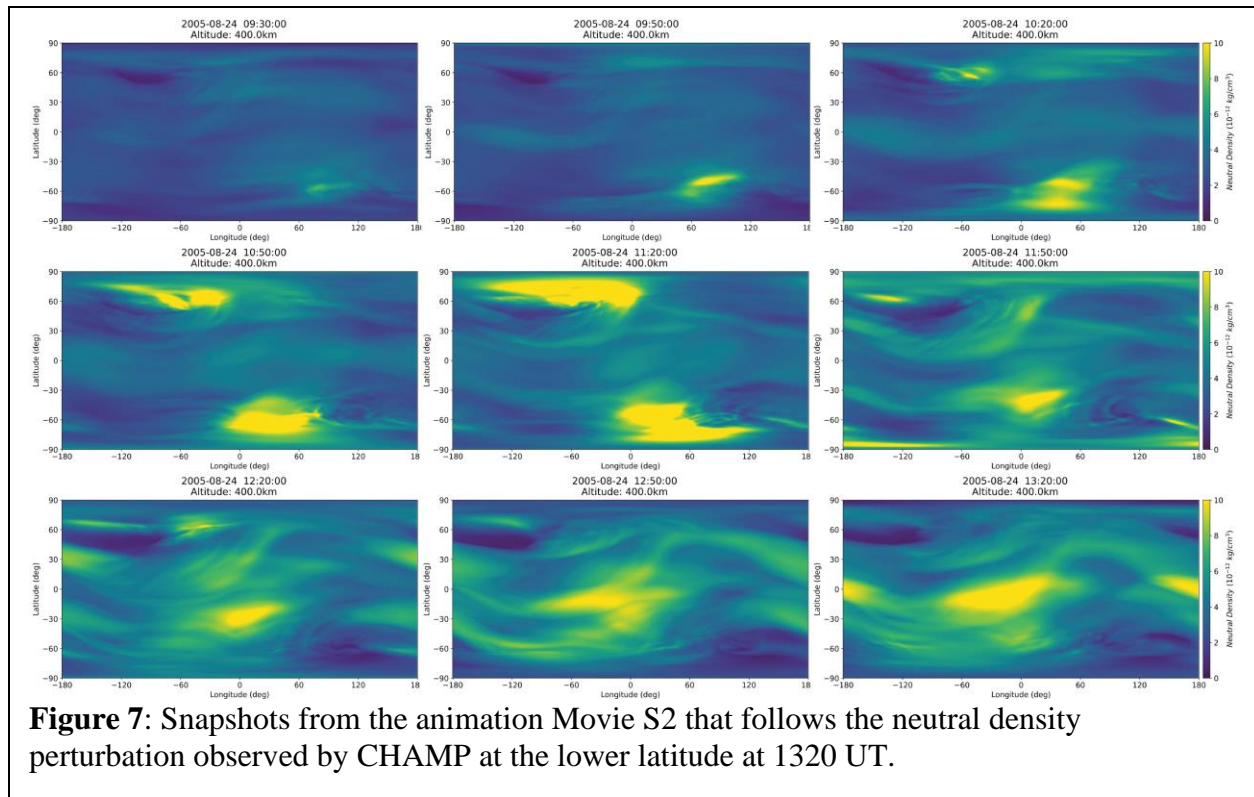
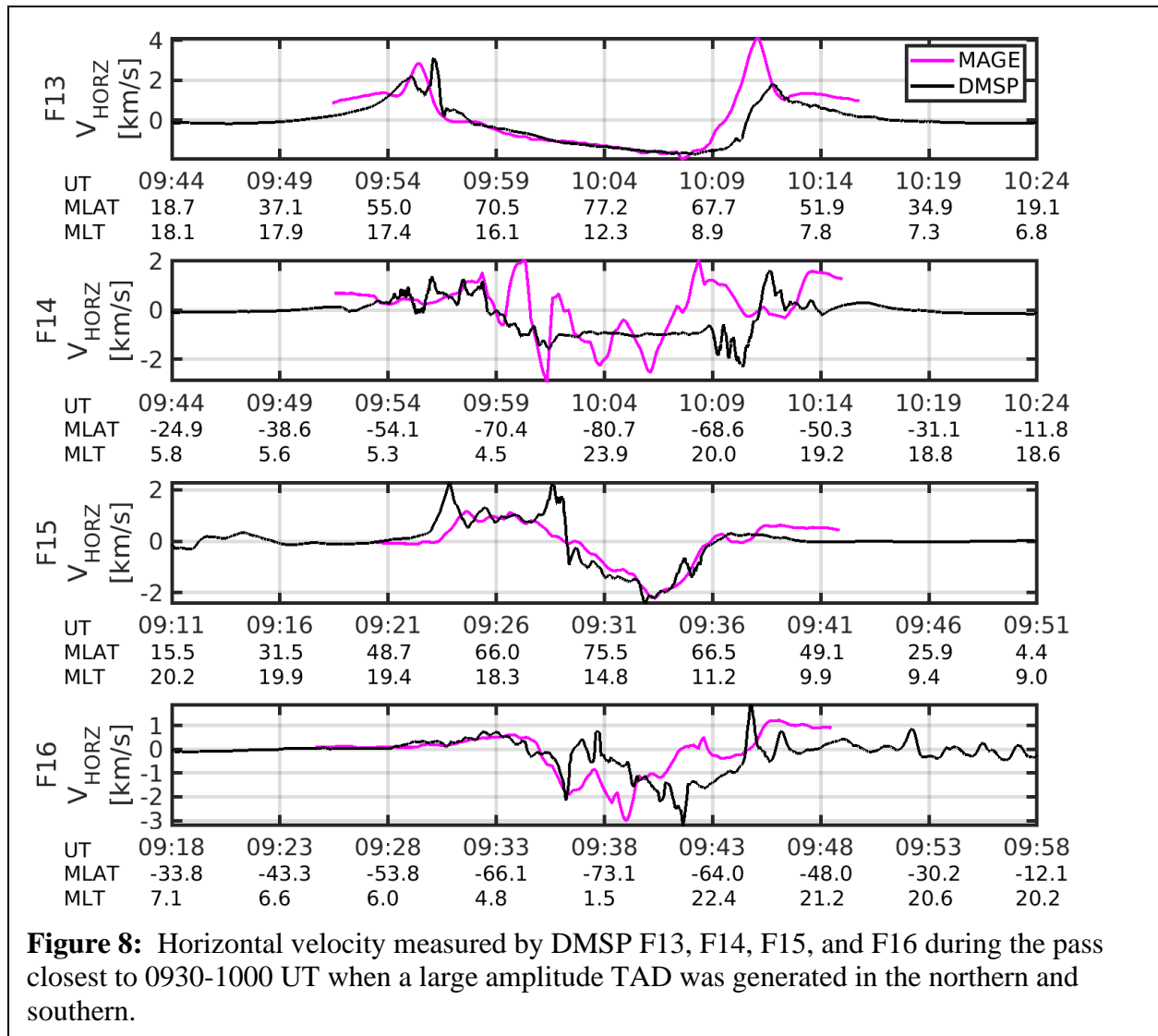


Figure 7: Snapshots from the animation Movie S2 that follows the neutral density perturbation observed by CHAMP at the lower latitude at 1320 UT.

379 CHAMP data. However, either the spatial timing or temporal timing of the TAD generated by
 380 MAGE is slightly misaligned, producing an underestimation of the GRACE and an overestimation
 381 of the CHAMP observations. For the height-integrated JH at 09:30 UT, the MAGE and WEIMER
 382 distributions are drastically different. The heating in WEIMER is distribution very broadly over a
 383 very large range of longitudes while the heating in MAGE is significantly more localized. This
 384 leads to WEIMER severely overestimating the enhancement in both the TAD source region at
 385 09:30 UT and at low latitudes at 13:20 UT as compared to the observed density perturbations by
 386 CHAMP. While WEIMER appears to capture the amplitude of the perturbation at 13:20 UT
 387 from GRACE better than MAGE, this is mostly likely purely coincidence. Indeed, subsequent
 388 orbits of GRACE in WEIMER near the same region intersects large perturbations that are not seen
 389 in observations and is grossly overestimated along the CHAMP track. This implies that the broad
 390 WEIMER distribution of JH coincidentally produces a perturbation that matches with observation
 391 at 13:23 UT along GRACE. Capturing all of these correctly is necessary as is done most of the
 392 time by MAGE.

393
 394 The global characteristic of neutral density perturbations is then dependent on not only the
 395 magnitude of the high latitude heating but also where the heating occurs, when the heating occurs,
 396 and the propagation speed and amplitude of the resulting high latitude disturbance. To further
 397 validate the accuracy of the MAGE Joule heating distribution, we compare the horizontal velocity
 398 measured by DMSP to those simulated by MAGE (Figure 8). The southern hemisphere passes
 399 (F14 and F16) have room for improvement. From Figure 6c, at around 09:30 UT in the southern
 400 hemisphere, there are multiple TADs being generated around this time that reach the northern
 401 hemisphere at around 12:00 UT. However, both models miss the neutral density perturbation in
 402 Figure 4 at 12:00 UT. The perturbations are likely from the southern hemisphere heating at 09:30



403 UT. For the northern hemisphere, both passes (F13 and F15) show that MAGE horizontal
 404 velocities agree surprisingly well with the observed. Overall, the capability to capture the
 405 generation, and evolution of the propagation speed and amplitude of the TAD that results in the
 406 observed low-latitude 13:20 UT neutral density enhancement represents a significant advancement
 407 and necessitates the need to have a coupled whole geospace model.

408 4 Conclusions

409 The MAGE coupled geospace model with high spatial resolving power in each region of geospace
 410 was used to simulate a geomagnetically active day of 24 August 2005 in which multiple
 411 thermospheric mass density enhancements are observed by CHAMP and GRACE. A fully coupled
 412 whole geospace model of MAGE with dynamically evolving high-resolution magnetosphere
 413 model and a high-resolution thermosphere-ionosphere model represents a significant improvement
 414 over using an empirical specification of high-latitude inputs of convection and precipitation in
 415 simulating Joule heating and the I-T responses. By flying virtual CHAMP and GRACE satellites
 416 through the simulations and compare with data, model performance and improvement was
 417 contrasted and quantified.

418 Our principal results are as follows:

- 419 • The coupled MAGE model reproduces both the magnitude and morphology of the storm-
420 time neutral density perturbations as measured by CHAMP and GRACE. The first
421 principles MAGE calculation of high latitude energy input from the magnetosphere to the
422 thermosphere and ionosphere performs significantly better than statistical empirical
423 specification of this input, especially during the main phase and recovery phases.
- 424 • Accurate description of both the distribution and magnitude of the localized Joule heating
425 at high-latitudes is critical to produce TADs with the correct properties to produce neutral
426 density enhancements not only at high-latitudes, but also in middle and low-latitudes that
427 match with CHAMP and GRACE observations
- 428 • Localized large neutral density enhancements in the mid to low-latitudes are oftentimes the
429 results of the intersection of multiple TADs generated in the high-latitudes

430 The MAGE model accurately captures both when and where the generation of TADs occurs and
431 also their propagation speeds and amplitudes, demonstrating that a high resolution, fully coupled
432 whole geospace model such as MAGE that can adequately resolve localized thermospheric heating
433 and the associated physics of MIT coupling, including dynamic changes in convection electric
434 fields and precipitation, is key to simulate the storm-time neutral density perturbations that are
435 fundamental to upper atmosphere dynamics and space weather application of satellite drag. This
436 is further reflected in the significant improvement in the RMSE and R^2 of MAGE compared to the
437 standalone TIEGCM driven by the WEIMER empirical specification. The neutral density
438 enhancements that are underestimated or missed by MAGE in the high-latitudes are most likely
439 related to the cusp-region heating sources that are not yet included in MAGE. These include other
440 sources of precipitation, such as direct entry cusp precipitation and broadband electron
441 precipitation (Zhang et al., 2015), and Alfvén wave heating (Hogan et al., 2020), that will be
442 implemented in the MAGE model in due course.

443 **Acknowledgments, and Data Sources**

444 CHAMP and GRACE data are archived at <http://tinyurl.com/densitysets>. IMF and Solar
445 wind data were provided by J.H. King, N. Papatashvili at AdnetSystems, NASA GSFC and
446 CDAWeb (<http://omniweb.gsfc.nasa.gov/>). We acknowledge support by the National Center for
447 Atmospheric Research (NCAR), a major facility sponsored by the National Science Foundation
448 under Cooperative Agreement No. 1852977 and NCAR System for Integrated Modeling of the
449 Atmosphere (SIMA) reinvestment fund. This work is supported by NASA LWS under grants
450 80NSSC21K0008, 80NSSC19K0071, 80NSSC19K0835, 80NSSC17K0013, 80NSSC19K0080,
451 80NSSC17K0679, and 80NSSC20K0356, DRIVE Science Center for Geospace Storms (CGS)
452 under grant 80NSSC20K0601, and O2R grant 80NSSC19K0241. Computing resources were
453 provided by NCAR's Computational and Information Systems Laboratory (CISL).

454
455 MAGE thermosphere-ionosphere results can be found at <https://doi.org/10.5281/zenodo.5587725>
456 . The REMIX results from MAGE can be found at <https://doi.org/10.5281/zenodo.5590561> .
457 Standalone TIEGCM results driven by Weimer can be found at
458 <https://doi.org/10.5281/zenodo.5590500> .

459
460

461 **References**

- 462 Billett, D. D., Perry, G. W., Clausen, L. B. N., Archer, W. E., McWilliams, K. A., Haaland, S., et
463 al. (2021). The relationship between large scale thermospheric density enhancements and the
464 spatial distribution of Poynting flux. *Journal of Geophysical Research: Space Physics*, 126,
465 e2021JA029205. <https://doi.org/10.1029/2021JA029205>
- 466 Bruinsma, S. L., & Forbes, J. M. (2007). Global observation of traveling atmospheric
467 disturbances (TADs) in the thermosphere. *Geophysical Research Letters*, 34, L14103.
468 <https://doi.org/10.1029/2007GL030243>
- 469 Bruinsma, S. L., & Forbes, J. M. (2009). Properties of traveling atmospheric disturbances
470 (TADs) inferred from CHAMP accelerometer observations. *Advances in Space Research*,
471 43(3), 369–376. <https://doi.org/10.1016/j.asr.2008.10.031>
- 472 Bruinsma, S. L., and J. M. Forbes (2009), Properties of traveling atmospheric disturbances
473 (TADs) inferred from CHAMP accelerometer observations, *Adv. Space Res.*, 23, 369–376,
474 doi:10.1016/j.asr.2008.10.031.
- 475 Bruinsma, S. L., and J. M. Forbes (2010), Large-scale traveling atmospheric disturbances
476 (LSTADs) in the thermosphere inferred from CHAMP, GRACE, and SETA accelerometer
477 data, *J. Atmos. Sol. Terr. Phys.*, 72, 1057–1066.
- 478 Bruntz, R., R. E. Lopez, S. K. Bhattarai, K. H. Pham, Y. Deng, Y. Huang, M. Wiltberger, and
479 J. G. Lyon (2012b), Investigating the viscous interaction and its role in generating the
480 ionospheric potential during the whole heliosphere interval, *J. Atmos. Sol. Terr. Phys.*, 83,
481 70–78, doi:10.1016/j.jastp.2012.03.016.
- 482 Burns, A. G., Killeen, T. L., Deng, W., Carignan, G. R., and Roble, R. G. (1995), Geomagnetic
483 storm effects in the low- to middle-latitude upper thermosphere, *J. Geophys. Res.*, 100(A8),
484 14673– 14691, doi:10.1029/94JA03232.
- 485 Connor, H. K., Zesta, E., Fedrizzi, M., Shi, Y., Raeder, J., Codrescu, M. V., & Fuller-Rowell, T.
486 J. (2016). Modeling the ionosphere-thermosphere response to a geomagnetic storm using
487 physics-based magnetospheric energy input: OpenGGCM-CTIM results. *Journal Space*
488 *Weather Space Climate*, 6(A25), 1–15. <https://doi.org/10.1051/swsc/2016019>
- 489 Dang, T., Lei, J., Wang, W., Burns, A., Zhang, B., & Zhang, S.-R. (2018). Suppression of the
490 polar tongue of ionization during the 21 August 2017 solar eclipse. *Geophysical Research*
491 *Letters*, 45, 2918– 2925. <https://doi.org/10.1002/2018GL077328>
- 492 Dang, T., Zhang, B., Lei, J., Wang, W., Burns, A., Liu, H-L., Pham, K., Sorathia, K. (2021). Az-
493 imuthal averaging-reconstruction filtering techniques for finite-difference general circulation
494 models in spherical geometry. *Geoscientific Model Development*, 1-30. doi:10.5194/gmd-
495 14-859-2021
- 496 Deng, Y., Fuller-Rowell, T. J., Ridley, A. J., Knipp, D., and Lopez, R. E. (2013), Theoretical
497 study: Influence of different energy sources on the cusp neutral density enhancement, *J.*
498 *Geophys. Res. Space Physics*, 118, 2340-2349, doi:10.1002/jgra.50197.
- 499 Fok, M.-C., Buzulukova, N. Y., Chen, S.-H., Glocer, A., Nagai, T., Valek, P., and Perez, J. D.
500 (2014), The Comprehensive Inner Magnetosphere-Ionosphere Model, *J. Geophys. Res. Space*
501 *Physics*, 119, 7522– 7540, doi:10.1002/2014JA020239.
- 502 Forbes, J. M., G. Lu, S. Bruinsma, S. Nerem, and X. Zhang (2005), Thermosphere density
503 variations due to the 15–24 April 2002 solar events from CHAMP/STAR accelerometer
504 measurements, *J. Geophys. Res.*, 110, A12S27, doi:10.1029/2004JA010856.

505 Guo, D., Lei, J., Ridley, A., & Ren, D. (2019). Low-density cell of the thermosphere at high
506 latitudes revisited. *Journal of Geophysical Research: Space Physics*, 124, 521– 533.
507 <https://doi.org/10.1029/2018JA025770>

508 Heelis, R. A., J. K. Lowell, and R. W. Spiro (1982), A model of the high-latitude ionosphere
509 convection pattern, *J. Geophys. Res.*, 87, 6339–6345, doi:10.1029/JA087iA08p06339.

510 Hogan, B., Lotko, W., & Pham, K. (2020). Alfvénic thermospheric upwelling in a global
511 geospace model. *Journal of Geophysical Research: Space Physics*, 125, e2020JA028059.
512 <https://doi.org/10.1029/2020JA028059>

513 Honkonen, I., Rastätter, L., Grocott, A., Pulkkinen, A., Palmroth, M., Raeder, J., Ridley, A. J.,
514 and Wiltberger, M. (2013), On the performance of global magnetohydrodynamic models in
515 the Earth's magnetosphere, *Space Weather*, 11, 313– 326, doi:10.1002/swe.20055.

516 Kelley, M. C., Knudsen, D. J., and Vickrey, J. F. (1991), Poynting flux measurements on a
517 satellite: A diagnostic tool for space research, *J. Geophys. Res.*, 96(A1), 201– 207,
518 doi:10.1029/90JA01837.

519 Kihn, E. A., Redmon, R., Ridley, A. J., and Hairston, M. R. (2006), A statistical comparison of
520 the AMIE derived and DMSP-SSIIES observed high-latitude ionospheric electric field, *J.*
521 *Geophys. Res.*, 111, A08303, doi:10.1029/2005JA011310.

522 Krall, J., Huba, J. D., Denton, R. E., Crowley, G., & Wu, T.-W. (2014). The effect of the
523 thermosphere on quiet time plasmasphere morphology. *Journal of Geophysical Research:*
524 *Space Physics*, 119, 5032–5048. <https://doi.org/10.1002/2014JA019850>

525 Krauss, S., Temmer, M., & Vennerstrom, S. (2018). Multiple satellite analysis of the Earth's
526 thermosphere and interplanetary magnetic field variations due to ICME/CIR events during
527 2003–2015. *Journal of Geophysical Research: Space Physics*, 123, 8884– 8894.
528 <https://doi.org/10.1029/2018JA025778>

529 Krauss, S., Temmer, M., Veronig, A., Baur, O., & Lammer, H. (2015). Thermosphere and
530 geomagnetic response to interplanetary coronal mass ejections observed by ACE and
531 GRACE: Statistical results. *Journal of Geophysical Research: Space Physics*, 120, 8848–
532 8860. <https://doi.org/10.1002/2015JA021702>

533 Lei, J., Thayer, J. P., Burns, A. G., Lu, G., and Deng, Y. (2010), Wind and temperature effects
534 on thermosphere mass density response to the November 2004 geomagnetic storm, *J.*
535 *Geophys. Res.*, 115, A05303, doi:10.1029/2009JA014754.

536 Liu, H., Lühr, H., and Watanabe, S. (2007), Climatology of the equatorial thermospheric mass
537 density anomaly, *J. Geophys. Res.*, 112, A05305, doi:10.1029/2006JA012199.

538 Liu, R., Lühr, H., & Ma, S.-Y. (2010). Storm-time related mass density anomalies in the polar
539 cap as observed by CHAMP. *Annales de Geophysique*, 28(1), 165–180. [www.ann-
540 geophys.net/28/165/2010/](http://www.ann-geophys.net/28/165/2010/). <https://doi.org/10.5194/angeo-28-165-2010>

541 Lopez, R. E., S. K. Bhattarai, R. Bruntz, K. Pham, M. Wiltberger, J. Lyon, Y. Deng, and Y.
542 Huang (2012), The role of dayside merging in generating the ionospheric potential during the
543 whole heliospheric interval, *J. Atmos. Sol. Terr. Phys.*, 83, 63–69,
544 doi:10.1016/j.jastp.2012.03.001.

545 Lu, G., Richmond, A. D., Lühr, H., and Paxton, L. (2016), High-latitude energy input and its
546 impact on the thermosphere, *J. Geophys. Res. Space Physics*, 121, 7108– 7124,
547 doi:10.1002/2015JA022294.

548 Matsuo, T., and Richmond, A. D. (2008), Effects of high-latitude ionospheric electric field
549 variability on global thermospheric Joule heating and mechanical energy transfer rate, *J.*
550 *Geophys. Res.*, 113, A07309, doi:10.1029/2007JA012993.

551 Mayr, H. G., I. Harris, F. A. Herrero, N. W. Spencer, F. Varosi, and W. D. Pesnell (1990),
552 Thermospheric gravity waves: Observations and interpretation using the transfer function
553 model (TFM), *Space Sci. Rev.*, 54, 297–375.

554 Merkin, V. G., and Lyon, J. G. (2010), Effects of the low-latitude ionospheric boundary
555 condition on the global magnetosphere, *J. Geophys. Res.*, 115, A10202,
556 doi:10.1029/2010JA015461.

557 Mukhopadhyay, A., Jia, X., Welling, D.T., Liemohn, M.W. (2021), Global
558 Magnetohydrodynamic Simulations: Performance Quantification of Magnetopause Distances
559 and Convection Potential Predictions, *Front. Astron. Space Sci.*, 8:637197. doi:
560 10.3389/fspas.2021.637197.

561 Oliveira, D. M., & Zesta, E. (2019). Satellite orbital drag during magnetic storms. *Space*
562 *Weather*, 17, 1510– 1533. <https://doi.org/10.1029/2019SW002287>

563 Prolls, G. (2011), Density perturbations in the upper atmosphere caused by the dissipation of
564 solar wind energy, *Surv. Geophys.*, 32, 101–195, doi:10.1007/s10712-010-9104-0.

565 Qian, L., Burns, A. G., Emery, B. A., Foster, B., Lu, G., Maute, A., ... & Wang, W. (2014). The
566 NCAR TIE-GCM: A community model of the coupled thermosphere/ionosphere system.
567 *Modeling the ionosphere-thermosphere system*, 201, 73-83.

568 Roble, R. G. & Ridley, E. C. (1987). An auroral model for the NCAR thermosphere general
569 circulation model (TGCM), *Annales Geophysicae*, 5A (6), 369-382.

570 Richmond, A. D. (2010), On the ionospheric application of Poynting's theorem, *J. Geophys.*
571 *Res.*, 115, A10311, doi:10.1029/2010JA015768.

572 Richmond, A., Ridley, E. C., & Roble, R. G. (1992). A thermosphere/ionosphere general
573 circulation model with coupled electrodynamics. *Geophysical Research Letters*, 19(6), 601–
574 604. <https://doi.org/10.1029/92GL00401>

575 Sorathia, K. A., Merkin, V. G., Panov, E. V., Zhang, B., Lyon, J. G., & Garretson, J., et al.
576 (2020). Ballooning-interchange instability in the near-Earth plasma sheet and auroral beads:
577 Global magnetospheric modeling at the limit of the MHD approximation. *Geophysical*
578 *Research Letters*, 47, e2020GL088227. <https://doi.org/10.1029/2020GL088227>

579 Sutton, E. K. (2011), Accelerometer-derived atmospheric densities from the CHAMP and
580 GRACE accelerometers: Version 2.3, Tech. Memo, Air Force Res. Lab., Kirtland Air Force
581 Base.

582 Toffoletto, F. R., S. Sazykin, R. W. Spiro, and R. A. Wolf (2003). Inner magnetosphere model-
583 ing with the Rice Convection Model, *Space Sci Rev*, 107, 175–196.

584 Vanhamäki, H., Yoshikawa, A., Amm, O., and Fujii, R. (2012), Ionospheric Joule heating and
585 Poynting flux in quasi-static approximation, *J. Geophys. Res.*, 117, A08327,
586 doi:10.1029/2012JA017841.

587 Wang, W., M. Wiltberger, A. G. Burns, S. Solomon, T. L. Killeen, N. Maruyama, and J. Lyon
588 (2004), Initial results from the CISM coupled magnetosphere-ionosphere-thermosphere
589 (CMIT) model: Thermosphere ionosphere responses, *J. Atmos. Sol. Terr. Phys.*, 66, 1425–
590 1441.

591 Wang, W., Talaat, E. R., Burns, A. G., Emery, B., Hsieh, S., Lei, J., and Xu, J. (2012),
592 Thermosphere and ionosphere response to subauroral polarization streams (SAPS): Model
593 simulations, *J. Geophys. Res.*, 117, A07301, doi:10.1029/2012JA017656.

594 Weimer, D. R. (2005), Improved ionospheric electrodynamic models and application to
595 calculating Joule heating rates, *J. Geophys. Res.*, 110, A05306, doi:10.1029/2004JA010884.

596 Wiltberger, M., Rigler, E., Merkin, V., & Lyon, J. (2017). Structure of high-latitude currents in
597 magnetosphere-ionosphere models. *Space Science Reviews*, 206, 575–598.
598 <https://doi.org/10.1007/s11214-016-0271-2>

599 Wiltberger, M., Rigler, E., Merkin, V., & Lyon, J. (2017). Structure of high-latitude currents in
600 magnetosphere-ionosphere models. *Space Science Reviews*, 206, 575–598.
601 <https://doi.org/10.1007/s11214-016-0271-2>

602 Xu, L. et al. (2008), A 2-D comparison of ionospheric convection derived from SuperDARN and
603 DMSP measurements, *Adv. Space Res.*, 42, 1259–1266.

604 Zhang, B., Lotko, W., Brambles, O., Wiltberger, M., Wang, W., Schmitt, P., and Lyon, J. (2012),
605 Enhancement of thermospheric mass density by soft electron precipitation, *Geophys. Res.*
606 *Let.*, 39, L20102, doi:10.1029/2012GL053519.

607 Zhang, B., Lotko, W., Brambles, O., Wiltberger, M., & Lyon, J. (2015). Electron precipitation
608 models in global magnetosphere simulations. *Journal of Geophysical Research: Space*
609 *Physics*, 120, 1035–1056. <https://doi.org/10.1002/2014JA020615>

610 Zhang, B., Sorathia, K. A., Lyon, J. G., Merkin, V. G., Garretson, J. S., & Wiltberger, M.
611 (2019a). GAMERA: A three-dimensional finite-volume MHD solver for non-orthogonal
612 curvilinear geometries. *The Astrophysical Journal Supplement Series*, 244(1), 20.
613 <https://doi.org/10.3847/1538-4365/ab3a4c>

614 Zhang B., Sorathia, K. A., Lyon, J. G., Merkin, V. G., & Wiltberger, M. (2019b). Conservative
615 averaging-reconstruction techniques (Ring Average) for 3-D finite-volume MHD solvers
616 with axis singularity. *Journal of Computational Physics*, 376, 276-294,
617 <https://doi.org/10.1016/j.jcp.2018.08.020>.

618